Cellular Oncology (2026) 49:47
https://doi.org/10.1007/s13402-026-01177-7

RESEARCH

Single-cell mapping of cholesterol metabolism reveals FDPS as a therapeutic vulnerability in hepatocellular carcinoma

Xupeng Yang[1] · Jiajun Li[2,3] · Yurong Wang[2,4] · Qiang Gao[1] · Mao Zhang[1]

Received: 9 November 2025 / Accepted: 7 February 2026

Abstract

Purpose Dysregulated cholesterol metabolism has emerged as a crucial driver of hepatocellular carcinoma (HCC) progression and immunotherapy resistance. This study aimed to delineate the single-cell landscape of cholesterol metabolism in HCC and identify key molecular determinants linking metabolic reprogramming to tumor aggressiveness and immune evasion.

Methods An integrative multi-omics approach combining bulk and single-cell RNA sequencing from multiple-center cohorts was employed. Metabolic activity scoring, high-dimensional weighted gene co-expression network analysis (hdWGCNA), and a five-model integrated machine learning strategy were applied to identify hub genes associated with cholesterol metabolism. Functional assays, including genetic silencing, metabolic profiling, and orthotopic mouse models with anti-PD-1 and FDPS inhibitor (alendronic acid), were used to validate mechanistic and therapeutic relevance.

Results Cholesterol metabolic activity was markedly elevated in HCC tumors and immune checkpoint blockade (ICB) non-responders, with pronounced intratumoral heterogeneity across malignant cell subpopulations. The enzyme Farnesyl Diphosphate Synthase (FDPS) emerged as a pivotal regulator, promoting tumor cell cholesterol metabolism and proliferation. Further functional experiments demonstrated that targeting FDPS suppressed tumor growth, reduced intracellular cholesterol levels and significantly enhanced anti-PD-1 efficacy in vivo, accompanied by increased lymphoid immune infiltration.

Conclusion Our findings establish FDPS-driven cholesterol metabolic reprogramming as a key mechanism of HCC malignancy and immunotherapy resistance. Targeting FDPS offers a promising strategy to potentiate immune checkpoint therapy and reshape metabolic vulnerabilities in liver cancer.

Keywords Hepatocellular carcinoma · Cholesterol metabolism · FDPS · Immunotherapy · Single-cell RNA sequencing

1 Introduction

Hepatocellular carcinoma (HCC) remains one of the most lethal malignancies worldwide. In 2019, HCC accounted for approximately 747,000 new cases globally, reflecting a 70% increase since 1990, with an estimated 480,000 deaths attributed to the disease [1]. Despite advances in surgical resection, and neo-adjuvant treatments such as immune checkpoint blockade (ICB), long-term survival rates remain dismal due to late diagnosis, tumor heterogeneity, and therapeutic resistance [2–4]. Therefore, a deeper understanding of the molecular mechanisms underlying HCC progression and treatment resistance is urgently needed.

Metabolic reprogramming is a hallmark of cancer and plays a central role in promoting tumor cell proliferation, immune evasion, and therapy resistance [5–7]. Among the

Xupeng Yang and Jiajun Li contributed equally to this work.

✉ Qiang Gao
gaoqiang@fudan.edu.cn

✉ Mao Zhang
zhang.mao@zs-hospital.sh.cn

[1] Department of Liver Surgery and Transplantation, and Key Laboratory of Carcinogenesis and Cancer Invasion (Ministry of Education), Liver Cancer Institute, Zhongshan Hospital, Fudan University, Shanghai 200032, China

[2] State Key Laboratory of Intelligent Cancer Biomarker Discovery and Translation, Department of Hepatopancreatobiliary Surgery, The First Affiliated Hospital of Wenzhou Medical University, Wenzhou 325015, China

[3] The Second School of Clinical Medicine, Wenzhou Medical University, Wenzhou 325017, China

[4] The First School of Clinical Medicine, Wenzhou Medical University, Wenzhou 325017, China

Published online: 18 February 2026

various metabolic alterations observed in cancer, dysregulation of cholesterol metabolism has garnered increasing attention [8]. Cholesterol is not only a structural component of cellular membranes but also a precursor for steroid hormones and signaling molecules [9–11]. Emerging evidence suggests that aberrant cholesterol biosynthesis and accumulation may contribute to tumorigenesis, particularly in liver cancers where lipid metabolic processes are tightly regulated [12]. Excessive dietary cholesterol contributes to the development of fatty liver associated liver cancer by altering the gut microbiota composition and associated metabolites [13]. Additionally, transmembrane protein 147 has been shown to aggravate HCC development by disrupting cholesterol homeostasis, suppressing ferroptosis, and promoting M2 polarization of tumor-associated macrophages (TAMs) [14]. However, the landscape of cholesterol metabolic activity in HCC at the single-cell level, as well as its association with malignant phenotypes and immunotherapy response, remains poorly defined.

Single-cell RNA sequencing is a powerful tool for dissecting the transcriptional heterogeneity of tumor ecosystems, enabling the identification of cell-type-specific metabolic programs [15, 16]. When combined with network-based approaches and machine learning, scRNA-seq can uncover functionally relevant gene modules and predictive biomarkers. In this study, we leveraged large-scale multi-center bulk and scRNA-seq datasets to investigate the role of cholesterol metabolism in HCC. Using an integrative strategy that combined metabolic activity scoring, high-dimensional weighted gene co-expression network analysis (hdWGCNA), and multi-model machine learning, we identified key gene signatures associated with elevated cholesterol metabolism in malignant cells [17–19]. Notably, Farnesyl Diphosphate Synthase (FDPS) emerged as a key gene driving cholesterol metabolic reprogramming in HCC, displaying overexpression in malignant cells, strong predictive power in all machine learning models, and serving as an independent indicator of poor prognosis. Knocking down FDPS significantly impaired cholesterol biosynthesis in HCC cells. Further functional and therapeutic investigations demonstrated that targeting FDPS not only suppressed tumor growth but also enhanced the efficacy of anti-PD-1 immunotherapy.

Collectively, our study provides a comprehensive map of cholesterol metabolism in HCC and identifies FDPS as a key metabolic gene associated with tumor progression and resistance to immune checkpoint blockade. These findings support the potential of targeting cholesterol biosynthesis as a complementary strategy to enhance immunotherapy efficacy in liver cancer.

2 Materials and methods

2.1 Data source

All datasets analyzed in this study are publicly accessible from reputable repositories. Raw single cell sequencing data was downloaded from the Genome Sequence Archive at the National Genomics Data Center (Beijing, China) under the BioProject ID PRJCA007744 [20]. Another processed scRNA-seq dataset, GSE149614, were downloaded from GEO data portal. Bulk RNA-seq datasets were retrieved from the TCGA-LIHC cohort via the UCSC Xena portal, the LIRI cohort from the ICGC data portal, the CHCC cohort from the NODE database, E-TABM-36 from EMBL's European Bioinformatics Institute [21, 22], and GSE14520 [23], GSE76427 [24], GSE84005 [25] and GSE54236 [26] from the GEO database. Collectively, these datasets provide a comprehensive resource for investigating transcriptomic alterations associated with HCC (Supplementary Table S1).

2.2 scRNA-seq data pre-processing and quality control

Single-cell RNA-seq data were aligned and quantified using the CellRanger toolkit (v3.1) against the GRCh38 reference genomes. Low-quality empty droplets were removed using the emptyDrops function of the dropletUtils R package (v1.10.3), which assesses whether the RNA content associated with a barcode is significantly different from the ambient background RNA in each library. Cells with a Benjamini-Hochberg-corrected false discovery rate (FDR) < 0.01 were retained for further analysis. Cells were retained if they contained fewer than 20% mitochondrial gene content, expressed more than 200 genes, and had between 200 and 6000 detected genes, appearing in at least three cells. After quality control, 360,046 cells were retained [20].

2.3 Cell clustering and annotation

We utilized Seurat R package (v4.4.0) and followed its pipeline for downstream analyses. The filtered scRNA-seq data were normalized and scaled using a linear regression model with the "Log-normalization" method. The top 2000 highly variable genes were identified through the "FindVariableFeatures" function. We then applied the "Harmony" package to correct for batch effects between samples and reduced dimensionality using Principal Component Analysis (PCA). Clustering of cells was performed with the "FindClusters" function, setting the resolution at 0.6. The dimensionality of each dataset was reduced using UMAP. Cell type identification was performed using the Signature-based Cell Type Annotation (SCTA) method, following the Hierarchical Cell

Annotation pipeline developed by Yang et al. [4]. This novel approach integrates cells' characteristic expression patterns with established canonical marker genes to achieve accurate and hierarchical classification of major and minor cell populations.

2.4 Consensus non-negative matrix factorization (cNMF)

GeneNMF R package (v0.9.1, https://github.com/carmonalab/GeneNMF) was used to infer gene expression programs from scRNA-seq data. The K-value was set as 6 to 10. The represented genes of distinct programs were subjected to an enrichment analysis using the "fgsea" R package (v1.30.0). Based on the enrichment results, six metaprograms (MPs) were identified and the remaining one was defined as a mixed program [27–30].

2.5 Metabolic activity analysis

Comparative analyses of metabolic activity across different groups were performed using the MetabolismExplorer R package (v0.1.0) for bulk RNA-seq datasets and the scMetabolism R package (v0.2.1) for single-cell RNA-seq datasets, respectively [31]. We followed the detailed instruction of the aforementioned R packages on github (scMetabolism: https://github.com/wu-yc/scMetabolism, MetabolismExplorer: https://github.com/StevenJiajunli/MetabolismExplorer, Supplementary Table S2).

2.6 Calculation of gene signature scores

For bulk RNA-seq data, the activity of each metabolic pathway was evaluated via GSVA R package (v1.46.0) using the Z-score transformation, defined as the mean expression of all genes in a given pathway normalized by their standard deviation across samples [32]. In terms of scRNA-seq data, individual cells were scored using the AddModuleScore function, which calculated the average expression levels of selected genes at the single-cell level and subtracted by the aggregated expression of control feature sets [33].

2.7 Empirical cumulative distribution analysis

Empirical cumulative distribution curves (eCDFs) were generated using the "stat_ecdf" function from the ggplot2 package in R. Distributions were plotted by group, with stepwise curves representing the cumulative fraction of values.

2.8 Differential analysis

For bulk RNA-seq data, differential expression analysis was performed using the limma R package (v3.54.2). Genes with a FDR < 0.05 and an absolute log2fold change > 1 were considered significantly differentially expressed. While for scRNA-seq data, differential expression analysis was conducted using the Seurat R package (v4.4.0). Cells were grouped by defined biological conditions, and differentially expressed genes (DEGs) between groups were identified using the likelihood-ratio test implemented in the "FindMarkers" function. The analysis was parallelized using the future R package (v1.31.0) to improve computational efficiency. Genes expressed in at least 25% of cells within either group, exhibiting a FDR < 0.05 and absolute log2fold change > 0.5 were considered significant.

2.9 High dimensional WGCNA (hdWGCNA)

We used hdWGCNA R package (v0.2.14) to identify HCC specific cholesterol metabolism related signatures. We followed the official pipeline released by Morabito et al., the hdWGCNA package designers, which is available on github repository (https://smorabit.github.io/hdWGCNA/) [18].

2.10 Screening of core genes involved in cholesterol metabolic reprogramming of HCC

A three-step pipeline was built for screening optimal genes involved in cholesterol metabolic reprogramming of HCC. Details of the three steps are as follows:

2.10.1 Step1: Collecting genes that are associated with cholesterol metabolic reprogramming

We first stratified malignant cells into three subgroups based on their cholesterol scores: LCholesterol (Score < −0.09676, bottom 25%), DTCholesterol (−0.09676 ≤ Score ≤ 0.14087, 25% to 75%), and HCholesterol (Score > 0.14087, top 25%). Then, we used single cell differential analysis (HCholesterol versus LCholesterol) and hdWGCNA to identify genes that was up-regulated and associated with HCholesterol subgroup, respectively. Subsequently, overlapping genes identified in the two analyses were collected and subjected to further screening.

2.10.2 Step2: Screening of core genes

With an intention to screen core genes involved, an integrative machine learning approach composed of five individual algorithms including LASSO, Boruta, GBM, RandomForest and XGBoost was utilized [34]. The malignant cells from

Zhang et al.'s single cell atlas were used to screen the optimal genes involved in cholesterol metabolic reprogramming.

The glmnet R package (v4.1-8) was used to perform LASSO regression, which introduces an L1 regularization term to penalize model complexity and shrink less informative feature coefficients toward zero, thereby selecting the most predictive genes. A binomial model was applied with the regularization parameter α set to 1, corresponding to LASSO penalization. Model tuning was conducted using 10-fold cross-validation to determine the optimal regularization parameter (λ). The value of λ that minimized the cross-validation error (λ_min) was selected, and the final model was refitted using this optimal λ. Genes with nonzero regression coefficients in the final LASSO model were considered as selected features for subsequent analyses.

A random forest model was constructed using the randomForest R package (v4.7-1.2) with 1,000 trees to ensure stable estimation. Model reproducibility was ensured by setting a fixed random seed. Variable importance was evaluated using the mean decrease in Gini index, and genes were ranked according to their importance scores. The top 20 genes were considered as key contributors to cholesterol metabolism-associated phenotypes and were used for downstream analyses.

The xgboost R package (v1.7.8.1) was used to implement the XGBoost algorithm, a gradient boosting framework capable of iteratively optimizing residual errors from previous trees while incorporating regularization to prevent overfitting. Key hyperparameters included a maximum tree depth of 3, a learning rate (eta) of 0.1, and 50 boosting rounds.

The gbm R package (v2.2.2) was applied to train GBM models, which build additive learners in a forward stagewise manner to sequentially correct residuals and refine feature importance rankings. Model parameters included 500 trees, an interaction depth of 3, and a learning rate (shrinkage) of 0.01. Five-fold cross-validation was applied to determine the optimal number of boosting iterations. Variable importance was assessed based on the relative influence of each gene, and genes were ranked accordingly. The top 20 genes identified by the GBM model were considered as important features and retained for subsequent analyses.

Finally, the Boruta R package (v8.0.0) was applied to identify all relevant features by iteratively comparing the importance of actual genes with their randomized "shadow" counterparts, thereby eliminating non-informative variables. The algorithm was run with 50 iterations, and genes confirmed or tentative by Boruta were retained as important features. These selected genes were subsequently used for downstream integrative analyses.

2.10.3 Step3: External validation

We examined whether the expression levels of selected genes varied according to the cholesterol metabolic state of the malignant cells through eCDF analysis using an external single cell cohort (GSE149614, HCholesterol versus LCholesterol malignant cells).

2.11 Survival analysis

Survival analysis was performed to evaluate the prognostic significance of candidate genes. Patients were stratified into high- and low-expression groups according to the median value of the corresponding gene or signature score. Kaplan Meier (KM) survival curves were generated using the survival (v3.7-0) and survminer (v0.4.9) R packages, and the hazard ratio (HR) and 95% confidence interval (CI) were calculated using univariate Cox proportional hazards regression.

2.12 Cell culture and establishment of stable knockdown cells

Murine hepatocellular carcinoma cell lines Hepa1-6 and Hep53.4 cells were descried in previous publication [4]. Cells were cultured in Dulbecco's modified Eagle's medium (DMEM, Gibco) supplemented with 10% fetal bovine serum (FBS, Gibco) and 1% penicillin–streptomycin at 37 °C in a humidified incubator with 5% CO_2. For genetic silencing, lentiviral vectors carrying FDPS-targeting short hairpin RNA (shFDPS) or a non-targeting control (shCtrl) were obtained from GeneChem (Shanghai, China). FDPS knockdown was achieved using lentiviral particles encoding shRNA sequences targeting mouse or human FDPS mRNA. After 48 h, successfully transduced cells were selected with 2 μg/mL puromycin for 5–7 days. Knockdown efficiency was verified by quantitative RT–PCR and immunoblotting before downstream assays.

2.13 Western blot analysis

Hepatocellular carcinoma cells were transduced with lentiviral vectors expressing shCtrl or three independent shRNAs targeting FDPS (shFDPS #1, shFDPS #2, and shFDPS #3). After selection with puromycin, cells were harvested for protein extraction.

Cells were lysed in RIPA buffer supplemented with protease inhibitor cocktail on ice for 30 min, followed by centrifugation at 12,000 × g for 10 min at 4 °C. The supernatants were collected, and protein concentrations were determined using a BCA assay.

Equal amounts of protein were resolved by SDS–PAGE and transferred onto PVDF membranes. Membranes were blocked with 5% non-fat milk in TBST for 1 h at room temperature and incubated overnight at 4 °C with a primary antibody against FDPS (abcam, ab153805) and GAPDH (proteintech, 60004-1-Ig). After washing, membranes were incubated with HRP-conjugated secondary antibodies for 1 h at room temperature. Protein bands were visualized using enhanced chemiluminescence (ECL), and images were captured using a digital imaging system.

2.14 RNA extraction and quantitative RT–PCR

Total RNA was extracted using TRIzol reagent (Invitrogen) according to the manufacturer's instructions. cDNA was synthesized with the PrimeScript RT reagent kit (Takara), and quantitative PCR was performed using SYBR Green Master Mix (Bio-Rad) on a QuantStudio 5 Real-Time PCR System (Applied Biosystems). The relative expression of target genes was normalized to β-actin using the $2^{-}\Delta\Delta Ct$ method. Primers for FDPS, SREBF2, HMGCR, MVK, IDI1, LDLR, INSIG1, ABCG1, CCND1, MYC, CDKN1A (p21), BCL2, and BAX were designed using Primer-BLAST and validated for specificity.

2.15 Cell proliferation assay

Proliferation dynamics were measured using the xCELLigence E-Plate 16 system. Cells (5×10^3 per well) were seeded and monitored for up to 72 h under standard culture conditions. The impedance-based cell index was normalized at the time of seeding. Growth curves were generated automatically, and proliferation rates were calculated from the slope of the exponential phase. Each experiment was performed in triplicate and repeated independently at least three times.

2.16 Cell migration assay

Real-time migration assays were performed using the xCELLigence RTCA DP system (Agilent Technologies). Briefly, 3×10^4 cells were seeded in serum-free medium in the upper chamber of CIM-Plate 16 wells, while the lower chamber contained medium with 10% FBS as chemoattractant. Cell index values were automatically recorded every 15 min for up to 30 h, and migration kinetics were analyzed using RTCA software.

2.17 Animal model construction and treatment

All animal experiments were performed in accordance with and approved Institutional Animal Careand Use Committee (lACUC). Six- to eight-week-old male C57BL/6 mice (purchased from Vital River Laboratory Animal Technology Co., Ltd.) were housed under specific pathogen–free conditions with a 12-hour light/dark cycle and ad libitum access to food and water. Hepa1-6 murine hepatocellular carcinoma cells (2×10^6 cells in 200 μL PBS) were injected orthotopically into liver. When tumors reached 80–100 mm^3, mice were randomized into four groups ($n = 6$–8 per group): (1) Saline control (vehicle, intraperitoneal injection), (2) αPD-1 (10 mg/kg, i.p., every three days), (3) Alendronic acid (1 mg/kg, i.p., every three days), (4) Combination therapy (αPD-1 plus alendronic acid, same dosing schedule). Tumor-bearing mice were anesthetized with 1.5% isoflurane and tumor volumes were measured every 4 days through high-resolution ultrasound imaging, which were calculated as (length × $width^2$)/2. And the body weight of mice was recorded concurrently.

2.18 Flow cytometry

Tumors were excised from mice, minced into small fragments, and enzymatically digested in RPMI-1640 containing collagenase and DNase I at 37 °C with gentle agitation. The resulting cell suspension was filtered through a 70 μm cell strainer to obtain single-cell suspensions. Red blood cells were lysed using ACK lysis buffer when necessary. Cells were washed with DPBS and resuspended in staining buffer (DPBS supplemented with 1% FBS). For surface staining, cells were incubated with the appropriate antibodies at room temperature for 30 min, followed by a wash with DPBS. A fixable viability dye (FVD780-eFluor™ 780, eBioscience, 65-0865-14) was used to exclude dead cells. For intracellular staining, cells were fixed and permeabilized using the Fixation/Permeabilization Kit (BD Biosciences, 554714) according to the manufacturer's instructions, followed by antibody staining in permeabilization buffer. The following anti-mouse antibodies were used: CD45-BUV395 (BD Biosciences, 564279), CD3-AF488 (BioLegend, 152322), CD4-PE/Cyanine5 (BioLegend, 100410), CD8a-BV650 (BioLegend, 100742), CD8a-BV785 (BioLegend, 100750), CD11b-BV510 (BioLegend, 101263), Ly6C-BV605 (BioLegend, 128035), F4/80-BV605 (BioLegend, 743281), Ly6G-AF700 (BD Biosciences, 561236), CD19-APC (BioLegend, 152409), NK1.1-PE (BioLegend, 108707), and CD11c-PE/Cyanine7 (BioLegend, 117317). Flow cytometry data were acquired on a BD LSRFortessa cytometer and analyzed using FlowJo software (BD). Immune cell populations were gated on live singlets and $CD45^+$ leukocytes prior to lineage-specific marker analysis.

2.19 Statistical analysis

Statistical analyses were performed using GraphPad Prism (v12.0) for experimental data and R (v4.2.1) for sequencing data and associated clinical variables. Comparisons between categorical variables were conducted using the χ^2 test or Fisher's exact test, while comparisons of continuous variables were performed using Student's t-test, Wilcoxon rank-sum test, or one-way ANOVA, as appropriate. Paired t-tests were used for paired comparisons. Survival analyses were performed using the log-rank test. A P value < 0.05 was considered statistically significant. Unless otherwise specified, all experiments were independently repeated at least three times.

3 Results

3.1 Single cell landscape of hepatocellular carcinoma

After applying the Harmony algorithm, the cellular distribution within each sample remained largely consistent, making them suitable for downstream analysis. A total of 16 distinct cell clusters were identified using a resolution parameter of 0.6 (Fig. 1A). Based on classical marker genes and hierarchical cell annotation pipeline, we successfully classified various cell populations, including malignant cells, endothelial cells, fibroblasts, neutrophil, mast cells, $CD4^+$ T cells, $CD8^+$ T cells, regulatory T cells (Tregs), NK cells, Plasma cells, B cells, dendritic cells (DCs), monocytes and macrophages (Fig. 1B and C). As expected, the tumor environment exhibited marked heterogeneity in cellular composition across samples (Fig. 1D).

We then applied a consensus non-negative matrix factorization algorithm to decipher transcriptional programs underlying tumor cell-intrinsic heterogeneity from 82 HCC samples (Fig. 1E). This analysis yielded ten gene signatures, which were subjected to hierarchical clustering, revealing five metaprograms (MPs) with discrete biological functions. MP1 was enriched for genes involved in proliferation (CCNB1, TOP2A, STMN1, TUBB). MP2 was characterized by drug metabolism and resistance genes (GSTA1, GSTA2, CYP2E1, CYP2C9). MP3 showed enrichment of antigen presentation and IFN-response (HLA-DRA, HLA-DRB1, ISG15, IFITM3), whereas MP4 was associated with hepatic metabolism (SERPINA4/5/6, FGA/B/G, APOE). MP5 comprised stress response related genes (HSPA1A, JUNB, DNAJB1), and MP6 was correlated with cellular senescence, charactered by ATF3 and CXCL2. These findings systematically delineate the cellular composition and tumor cell-intrinsic functional heterogeneity in HCC.

3.2 Altered cholesterol metabolism is associated with tumor malignancy and ICB resistance

MetabolismExplorer was utilized to investigate metabolic reprogramming in bulk RNA-seq cohorts and it defined that cholesterol metabolic activity was upregulated in HCC samples versus normal samples and in samples of ICB non-responders (NR) versus responders' (R). As depicted in Fig. 2A, analysis across five independent datasets including HCC and corresponding normal samples (CHCC, TCGA, GSE14520, GSE76427 and GSE84005) consistently demonstrated significantly elevated cholesterol metabolism scores in tumor tissues (T) compared to matched normal tissues (N). More importantly, in the 2023 Nanjing cohort, ICB non-responders exhibited markedly higher cholesterol metabolism activity compared to responders, suggesting a potential link between cholesterol metabolic rewiring and immunotherapy resistance.

To characterize the cell-type-specific patterns of cholesterol metabolism, single-cell transcriptomic analysis was performed. Malignant cells exhibited substantially higher cholesterol metabolism scores than non-malignant immune and stromal cell types (Fig. 2B-D). As the scRNA-seq NMF analysis shown significant inter- and intra-tumoral heterogeneity between and within HCC samples, we further investigated the heterogeneous cholesterol metabolic activity in HCC. Based on the distribution of cholesterol metabolism scores in malignant cells, we classified HCC into three subgroups: High Cholesterol Metabolism (HCholesterol, Score > 0.14087, top 25%), Low Cholesterol Metabolism (LCholesterol, Score < -0.09676, bottom 25%), and an intermediate group (Dynamic Transitioning Cholesterol Metabolism, DTCholesterol). This stratification reflects the metabolic heterogeneity of tumor cells and enables downstream analysis of their molecular and functional differences (Fig. 2E and F).

To explore the molecular characteristics of these subgroups, differential expression analysis was performed by integrating single-cell and bulk RNA sequencing data (Supplementary Table S3, S4). HCholesterol malignant cells were enriched for genes involved in cholesterol biosynthesis and transport, including SQLE, HMGCS1, FDPS, SCD, and APOA2, while LCholesterol cells expressed epithelial differentiation markers such as KRT19, SPINK1, and metallothioneins (MT1X, MT1G) (Fig. 2G). Correlation analysis revealed that cholesterol metabolism was positively associated with KRAS-upregulated gene signatures ($R = 0.302$, $P < 0.001$). Notably, cholesterol homeostasis showed weaker or inverse associations with these oncogenic programs, indicating the specific role of metabolic activation rather than balance in supporting tumor progression (Fig. 2H).

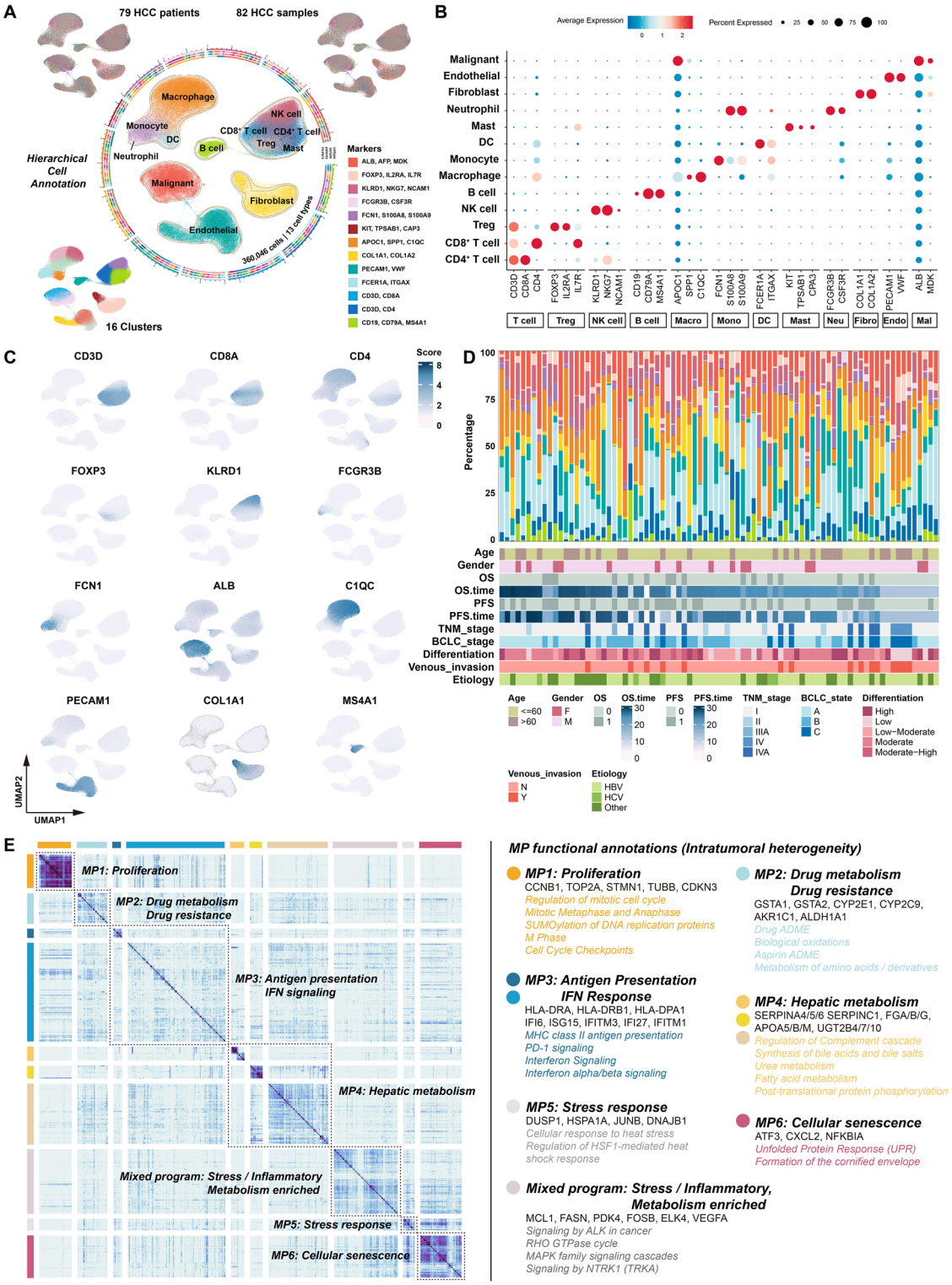

Fig. 1 Single-cell transcriptomic landscape of HCC. (**A**) UMAP visualization of 82 HCC samples from 79 patients revealed 16 major cell clusters, hierarchically annotated into malignant, immune, and stromal lineages. (**B**) Dot plot showing the expression and proportion of canonical marker genes across major cell types. (**C**) Feature plots displaying representative markers confirming cell-type identities. (**D**) Distribution of cell types across patients and clinical features, including age, gender, stage, differentiation, venous invasion, and etiology. (**E**) Identification of six malignant cell metaprograms (MPs) capturing distinct functional states

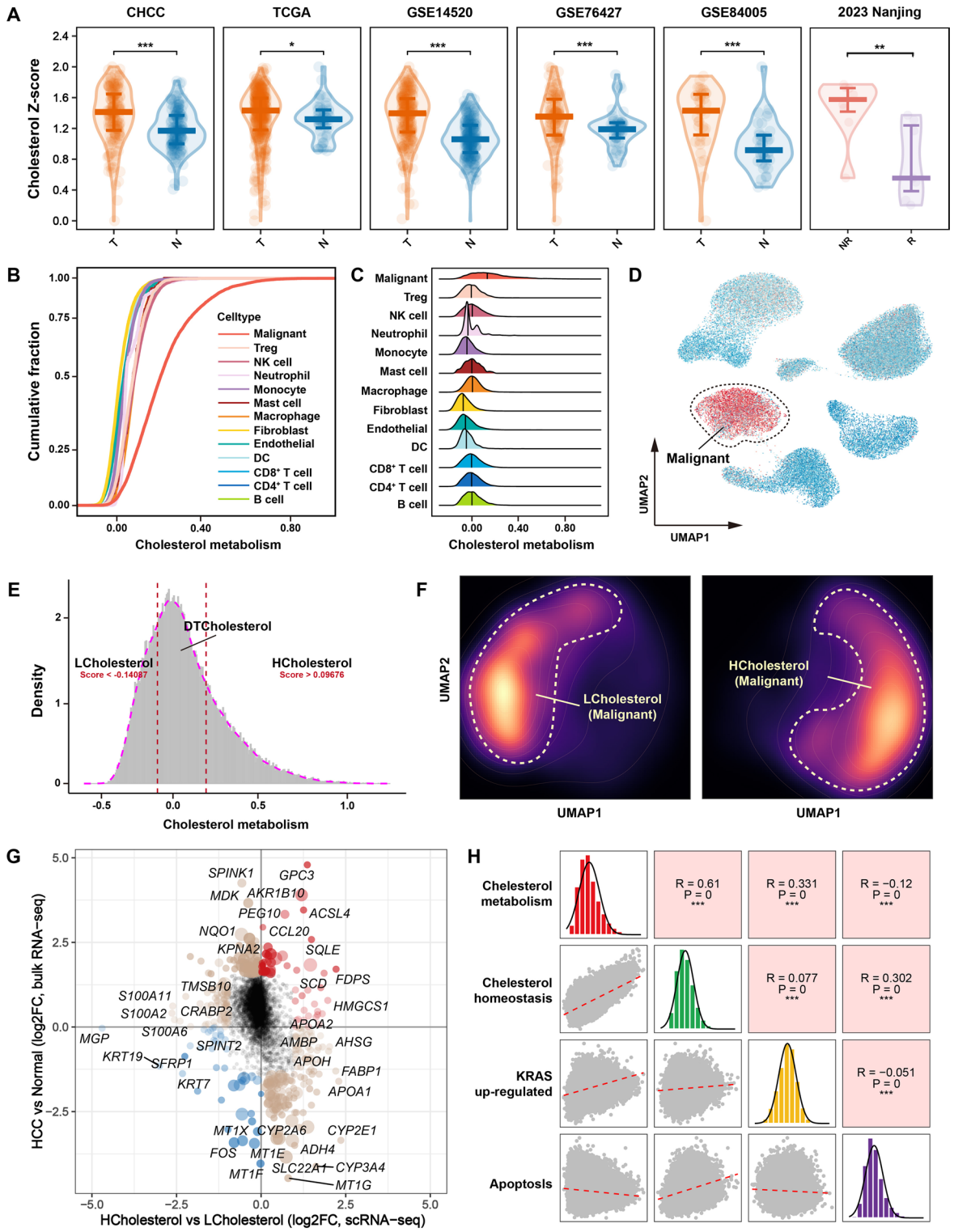

3.3 HdWGCNA and differential analysis reveals HCholesterol-related genes

A combination of hdWGCNA and multiple machine learning models, including LASSO, RandomForest, Boruta, GBM, and XGBoost, was applied to collect and refine HCholesterol-related signatures, with an intention to figure out core drivers of cholesterol metabolic reprogramming in HCC (Fig. 3A).

To construct a reliable co-expression network within the HCholesterol cell subset, an optimal soft-thresholding power was determined using scale-free topology criteria

Fig. 2 Altered cholesterol metabolism is associated with tumor malignancy and immunotherapy resistance. (**A**) Cholesterol metabolism activity was significantly elevated in tumor tissues compared with adjacent normal tissues across multiple HCC cohorts. (**B**, **C**) Distribution of cholesterol metabolism scores across major cell types, with malignant cells showing the highest enrichment. (**D**) Malignant cells with elevated cholesterol metabolism activity. (**E**) Density plot defining malignant cell subgroups with low (LCholesterol) and high (HCholesterol) cholesterol metabolism. (**F**) UMAP heatmaps illustrating spatial distribution of LCholesterol and HCholesterol malignant populations. (**G**) Correlation between cholesterol-related metabolic differences in scRNA-seq (HCholesterol vs. LCholesterol) and bulk RNA-seq (HCC vs. normal) datasets, highlighting shared metabolic genes. (**H**) Correlation matrix showing relationships between cholesterol metabolism, cholesterol homeostasis, KRAS upregulation, and apoptosis signatures across malignant subpopulations. *P*-values were determined by Wilcoxon rank-sum test in (**A**). Simple linear regression was applied for *P*-value and correlation analyze the Spearman r in (**H**). *, $p<0.05$; **, $p<0.01$; ***, $p<0.001$

(Soft Power Threshold = 7, Fig. 3B). The resulting hdWGCNA dendrogram revealed multiple distinct gene modules, each assigned a unique color (Fig. 3C). These modules were mapped onto the UMAP embedding of malignant cells, showing clear spatial heterogeneity in module activation patterns (Fig. 3D). Key representative genes within each module, referred to as "Cho_states" (e.g., Cho_state-M1 to M9), were prioritized based on their Mean Absolute Error (MAE) scores from machine learning models (Fig. 3E). Modules Cho_state-M1, Cho_state-M7 and Cho_state-M9 were particularly enriched in the HCholesterol group, as demonstrated by the module-trait correlation matrix (Fig. 3F), indicating a strong association with elevated cholesterol metabolism.

We then conducted functional enrichment analysis to further investigate the biological relevance of genes in both HCholesterol-specific co-expression modules and genes upregulated in HCholesterol versus LCholesterol malignant cells ($n = 178$, Supplementary Table S5). Protein-protein interaction (PPI) network analysis highlighted dense connectivity among the intersected genes (Fig. 3G), while pathway enrichment revealed significant involvement in metabolic processes such as steroid metabolism, small molecule catabolic processes, and PPAR signaling (Fig. 3G).

3.4 FDPS is aberrantly upregulated in hepatocellular carcinoma and predicts unfavorable patient outcomes

The 178 genes identified by hdWGCNA and single-cell differential analysis were prioritized according to their selection frequency across the five aforementioned machine learning algorithms applied to comparisons between HCholesterol and LCholesterol malignant cells. 154 genes with non-zero regression coefficients were included in the final LASSO model while 155 genes were selected by Boruta algorithm. A total of 13 shared genes were selected by the five algorithms, namely SERPINC1, ALB, PLG, TM7SF2, APOC3, APOA1, CYP2E1, HP, SQLE, FDPS, IDI1, DHCR7, HMGCS1 (Fig. 4A, Supplementary Figure S1). The results of the ECDF analysis comparing the expression levels of these 13 genes between HCholesterol and LCholesterol malignant cells in an independent scRNA-seq cohort (GSE149614) are shown in Supplementary Figure S2.

Among the top-ranked genes, FDPS (Farnesyl diphosphate synthase) emerged as a particularly robust candidate. It was strongly associated with cholesterol metabolism scores across multiple RNA-seq cohorts, consistently selected by all five machine learning algorithms, and significantly upregulated in malignant cells compared with normal tissues across several HCC cohorts, including TCGA, CHCC, LIRI, GSE14520, GSE76427, and GSE84005 (Fig. 4B and Supplementary Fig. S3). Survival analyses further confirmed that FDPS was an independent prognostic factor, underscoring the clinical relevance of FDPS activation in HCC (Fig. 4C).

To determine how FDPS regulates proliferative transcriptional networks in tumor cells, we profiled the expression of key genes involved in the cell-cycle control following FDPS knockdown (shFDPS). To validate FDPS knockdown efficiency, western blot analysis using three independent shRNAs demonstrated that shFDPS #1 and shFDPS #2 achieved the most efficient and consistent suppression of FDPS protein expression, and were therefore selected for all subsequent experiment (Fig. 4D). Quantitative RT-PCR analysis revealed a broad metabolic reprogramming in shFDPS cells relative to wild-type controls. FDPS loss profoundly affected genes governing cell proliferation and apoptosis (Fig. 4E). Cyclin D1 (CCND1) expression was significantly reduced, whereas the cyclin-dependent kinase inhibitor CDKN1A (p21) and the pro-apoptotic effector BAX were robustly up-regulated. In contrast, expression of MYC and BCL2 remained largely unchanged, suggesting that FDPS knockdown selectively impacts prenylation-dependent signaling rather than global transcriptional programs. In addition, FDPS knockdown resulted in a significant reduction in total cellular cholesterol content (Fig. 4F). To further evaluate the functional consequences of FDPS knockdown, we assessed tumor cell migration and proliferation in two murine hepatocellular carcinoma cell lines. The result showed FDPS knockdown significantly suppressed tumor cell growth and migratory capacity over time in both cell lines compared with wild-type controls (Fig. 4G). Together, these findings establish that FDPS is aberrantly activated in HCC, drives oncogenic metabolism, and promotes aggressive cellular behavior, implicating FDPS as a potential therapeutic target in liver cancer.

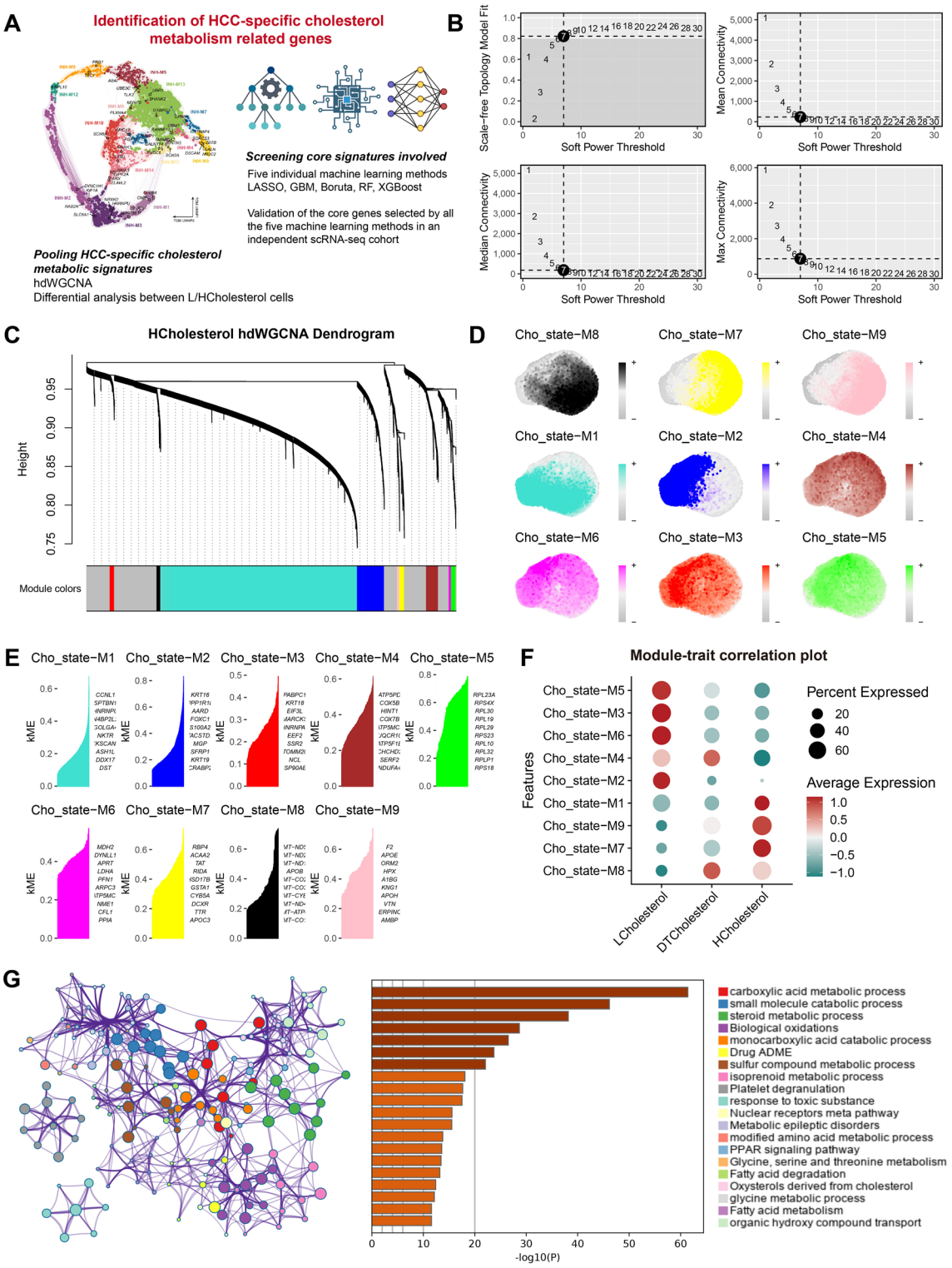

Fig. 3 Identification of HCC-specific cholesterol metabolism-related gene modules. (**A**) Workflow for identifying HCC-specific cholesterol metabolic signatures using high dimension WGCNA (hdWGCNA), differential analysis and integrated machine learning. (**B**) Selection of the soft-thresholding power for network construction. (**C**) hdWGCNA dendrogram showing gene co-expression modules in HCholesterol malignant cells. (**D**) UMAP visualization of module eigengene expression across malignant subpopulations. (**E**) Top hub genes within each cholesterol metabolic module. (**F**) Correlation of each module with LCholesterol, DTCholesterol, and HCholesterol malignant states. (**G**) Protein-protein interaction (PPI) network and enrichment analysis of the shared genes between module genes and up-regulated genes in HCholesterol versus LCholesterol malignant cells

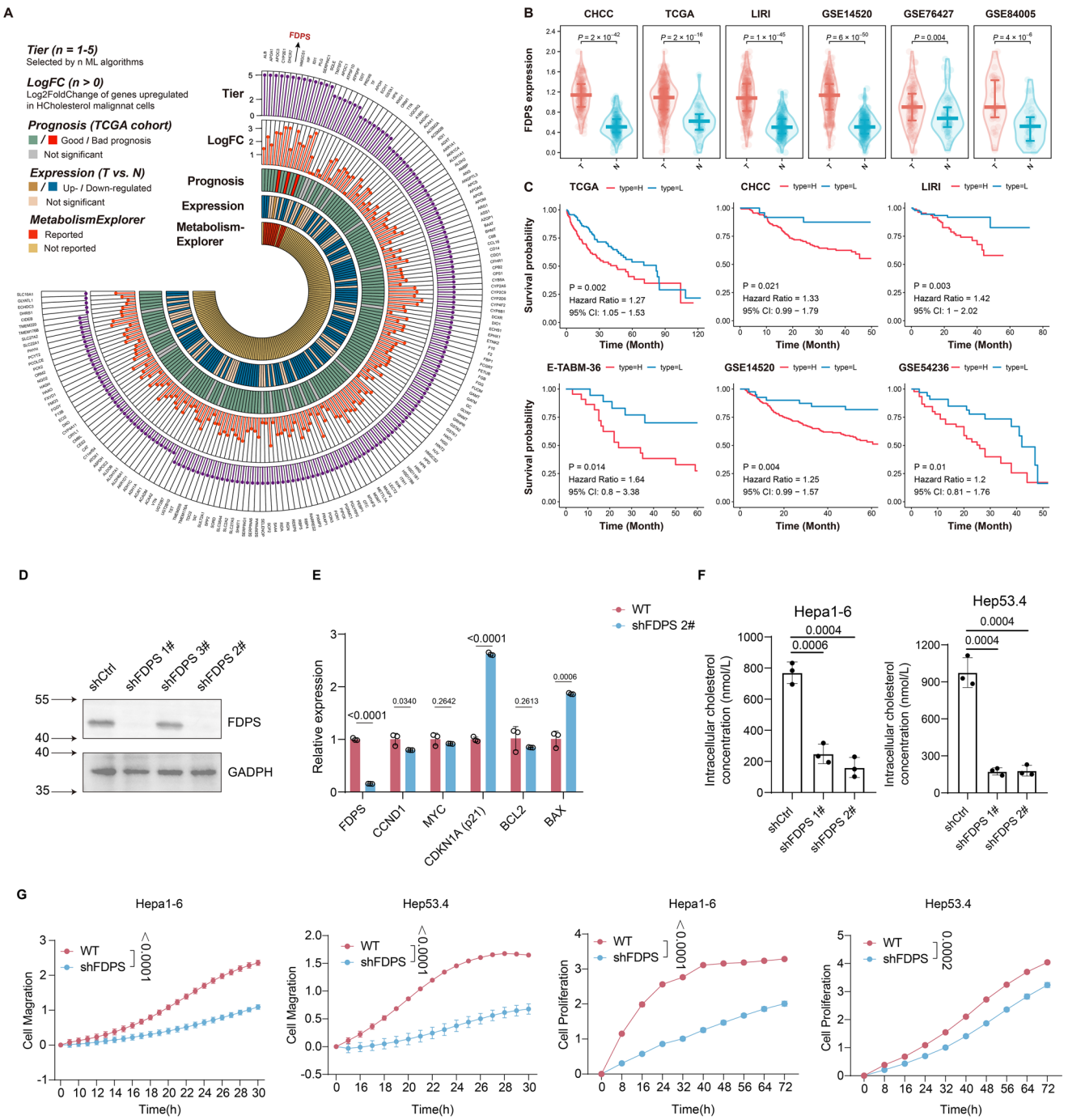

Fig. 4 FDPS is a crucial gene involved in cholesterol metabolic reprogramming in HCC. (**A**) Screening of core genes involved in cholesterol metabolic reprogramming in HCC. (**B**) FDPS expression levels were up-regulated in HCC samples versus normal samples. (**C**) Higher FDPS expression levels were associated with worse prognosis. (**D**) Validation of FDPS knockdown at the protein level. (**E**) FDPS knocking down significantly influenced the expression levels of transcription factors. (**F**) FDPS knockdown reduces intracellular cholesterol levels in HCC cells. (**G**) FDPS knocking down inhibited cell migration and proliferation. *P*-values were determined by Wilcoxon rank-sum test in (**B**), Log-rank test was applied in (**C**), one-way Anova in (**F**) and two-tailed unpaired Student's t-test (**D**, **G**). ns, $p > 0.05$; *, $p < 0.05$; **, $p < 0.01$; ***, $p < 0.001$. HR, hazard ratio. WT, wild type

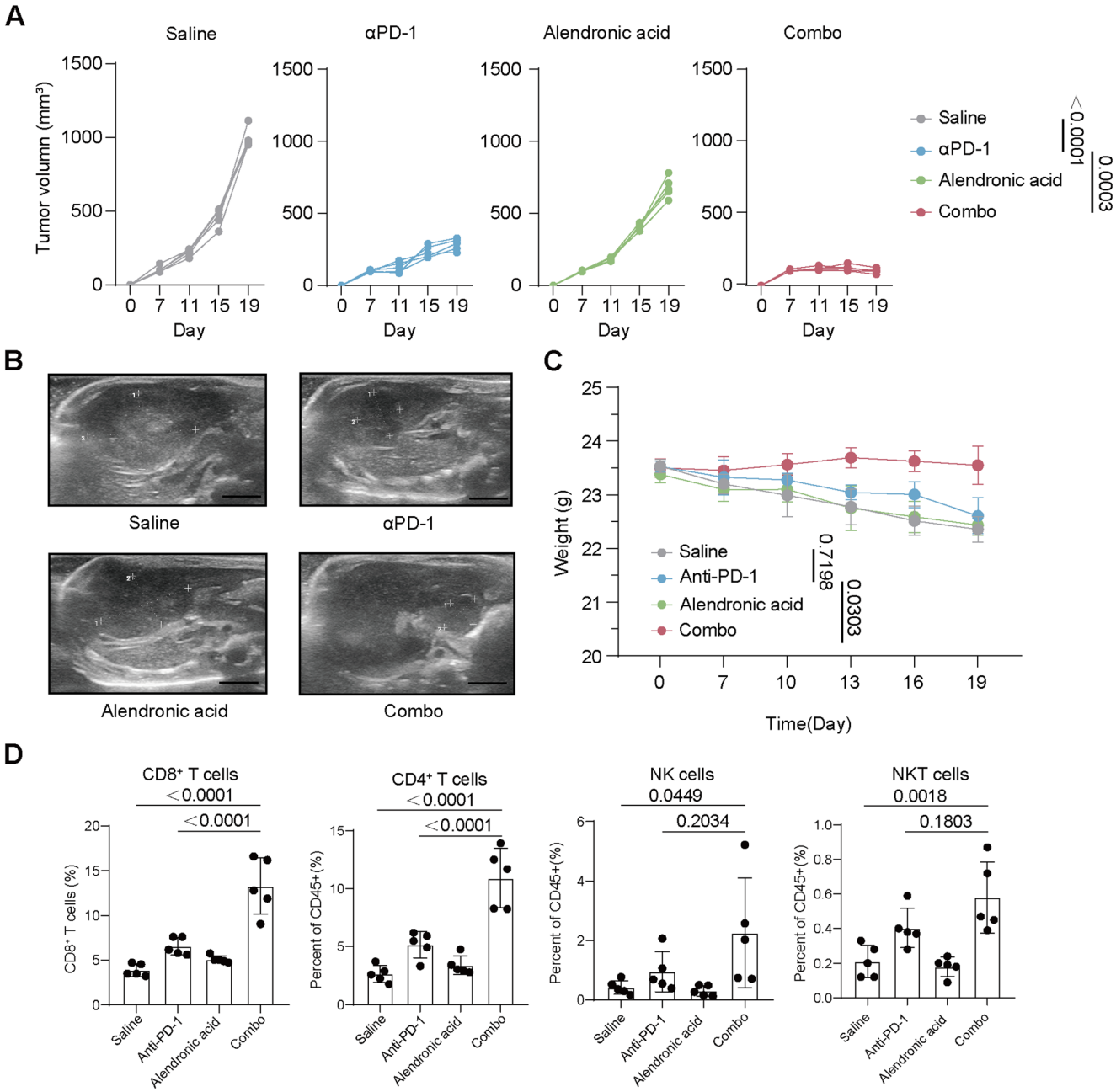

Fig. 5 FDPS inhibition enhanced immunotherapy efficacy. (**A**, **B**) Combined treatment with the FDPS inhibitor (alendronic acid) and anti-PD-1 antibody significantly reduced tumor volume. Scale bar =6 mm. (**C**) Combined treatment caused minimal changes in mouse body weight. (**D**) FDPS inhibition reshapes the tumor immune microenvironment and enhances lymphoid immune infiltration in combination with anti–PD-1 therapy. *P*-values were determined by one-way ANOVA test in (**A**) and (**D**). ns, $p>0.05$; ***, $p<0.001$

3.5 Targeting FDPS sensitizes the efficacy of PD-1 Blockade in hepatocellular carcinoma

To determine whether inhibition of the mevalonate pathway could potentiate immune checkpoint blockade, we established an orthotopic hepatocellular carcinoma (HCC) model using murine Hepa1-6 cells in immunocompetent C57BL/6 mice (Fig. 5A-B). The growth of orthotopic tumors was longitudinally monitored by ultrasound imaging until tumors volume of mice in any treatment group reached the ethical limit. Once tumors reached approximately 100 mm³, mice were randomly assigned to four treatment groups: saline control, anti-PD-1 antibody (αPD-1), alendronic acid (FDPS inhibitor), or their combination. The result showed tumor growth progressed rapidly in saline-treated controls, whereas both αPD-1 and alendronic acid monotherapies

modestly delayed tumor expansion. In striking contrast, the combination treatment elicited a profound and sustained suppression of tumor growth throughout the observation period, resulting in the smallest mean tumor volume among all groups (Fig. 5A-B). This cooperative effect suggests that pharmacologic inhibition of FDPS markedly sensitizes tumors to αPD-1 immunotherapy. Importantly, longitudinal monitoring of body weight revealed no significant difference among groups (Fig. 5C), indicating that the combined treatment was well tolerated and did not induce overt systemic toxicity.

Multicolor flow cytometry analysis of tumor-infiltrating immune cells revealed that combined treatment with alendronic acid and anti–PD-1 antibody markedly reshaped the tumor immune microenvironment (Fig. S4A). Compared with saline or anti–PD-1 antibody groups, the combination treatment significantly increased the infiltration of $CD8^+$ T cells and $CD4^+$ T cells among $CD45^+$ leukocytes (Fig. 5D). In parallel, NK cells and NKT cells were also significantly elevated in the combination group compared with the saline group, indicating enhanced innate and adaptive immune activation (Fig. 5D). By contrast, neutrophils were reduced following combination treatment, whereas the overall proportion of macrophages was not significantly altered across groups (Fig. S4B). These results indicate that FDPS inhibition preferentially promotes lymphoid immune infiltration and activation rather than broadly remodeling myeloid populations.

To assess potential off-target effects, major organs were harvested for histopathological analysis. Hematoxylin and eosin (H&E) staining of lung, heart, spleen, and kidney tissues showed preserved architecture without inflammatory infiltrates, necrosis, or fibrotic lesions across all treatment groups (Fig. S4C). These data collectively demonstrate that concurrent blockade of PD-1 signaling and FDPS enzymatic activity achieves potent antitumor efficacy while maintaining systemic safety.

Mechanistically, the enhanced therapeutic effect of the combination likely reflects dual targeting of tumor-intrinsic and immune-mediated pathways: FDPS inhibition disrupts cholesterol metabolism and tumor proliferation, while PD-1 blockade relieves T-cell exhaustion within the tumor microenvironment. Together, these complementary mechanisms converge to produce robust tumor control in vivo.

4 Discussion

Metabolic reprogramming is an important hallmark of cancer that enables tumor cells to meet the demands of rapid proliferation, survival under stress, and immune evasion [35, 36]. While the Warburg effect, characterized by enhanced glycolysis even under normoxic conditions, has been the most extensively studied metabolic alteration in cancer, recent studies have broadened our understanding of cancer metabolism to include lipid and cholesterol biosynthesis other important components of tumor metabolic plasticity [37, 38]. However, most existing studies have evaluated cholesterol metabolism either at the bulk transcriptomic level or by focusing on single pathways or enzymes, which limits our ability to capture the full complexity and heterogeneity of this metabolic program within tumors [8, 39]. These approaches often overlook the diverse metabolic states of individual cell populations and the potential interactions between metabolic phenotypes and immunotherapy responses [9, 40].

In this study, we addressed these gaps by integrating single-cell and bulk transcriptomic data to construct a high-resolution map of cholesterol metabolism in HCC. Our analysis revealed not only elevated cholesterol metabolic activity in tumor tissues and ICB non-responders but also striking intratumoral metabolic heterogeneity among malignant cells. This led to the identification of transcriptionally distinct subgroups, HCholesterol, LCholesterol, and DTCholesterol, each exhibiting unique gene expression programs and potential associations with therapy resistance. These findings underscore the need to assess cancer metabolism at the single-cell level to better understand its clinical and immunological implications. To further dissect the molecular underpinnings of cholesterol metabolic heterogeneity in HCC, hdWGCNA to malignant cells with high cholesterol activity, followed by an integrative machine learning approach comprising LASSO, Random Forest, Boruta, GBM, and XGBoost algorithms. This strategy enabled us to prioritize 178 HCholesterol-related genes with consistent differential expression patterns and prognostic relevance. Among them, FDPS emerged as a particularly robust candidate, being selected by all five models, significantly overexpressed in tumor tissues across multiple independent cohorts, and strongly associated with poor patient survival.

Functionally, FDPS catalyzes the production of geranyl pyrophosphate and farnesyl pyrophosphate from isopentenyl pyrophosphate and dimethylallyl pyrophosphate. The resulting product, farnesyl pyrophosphate, is a key intermediate in cholesterol and sterol biosynthesis, a substrate for protein farnesylation and geranylgeranylation, and a ligand or agonist for certain hormone receptors and growth receptors [41]. In our study, knocking down FDPS impaired cholesterol biosynthesis, suppressed tumor cell proliferation, enhanced T cell infiltration and sensitized tumors to anti-PD-1 immunotherapy. Also, the positive association between cholesterol metabolic potency and KRAS-upregulated gene signatures suggests that metabolic reprogramming and oncogenic RAS signaling are mechanistically

coupled rather than mutually exclusive. FDPS controls the generation of isoprenoid intermediates required for KRAS prenylation and activation, thereby linking sterol metabolism to RAS/MEK/ERK signaling. In this context, FDPS-driven metabolic reprogramming may promote immune evasion through both cholesterol-dependent membrane effects and prenylation-dependent oncogenic signaling, together shaping resistance to immune checkpoint blockade. Given the availability of clinically approved FDPS inhibitors (e.g., Alendronic acid [42, 43]), our findings provide a strong rationale for repurposing these agents in combination with immunotherapy to overcome ICB resistance.

Our findings also reinforce and expand upon previous studies that have implicated cholesterol metabolism in cancer progression and immune regulation. First, our study identified a panel of key metabolic enzymes that potentially drive cholesterol biosynthetic reprogramming in HCC. Among the top-ranked genes enriched in HCholesterol malignant cells, we observed upregulation of several core enzymes in the cholesterol biosynthesis and transportation pathways, including FDPS, SQLE (Squalene Monooxygenase), SCD (Stearoyl-CoA Desaturase), HMGCS1 (3-Hydroxy-3-Methylglutaryl-CoA Synthase 1), and APOA2 (Apolipoprotein A2) [44]. Many of these genes have been independently implicated in hepatocarcinogenesis or lipid metabolic dysregulation in previous studies. For instance, SQLE and its metabolite, cholesterol, impaired $CD8^+$ T cell activity by inducing mitochondrial dysfunction, which eventually led to ICB resistance [45]. Apart from that, Li et al. figured out that CSN6-SPOP-HMGCS1 axis promotes HCC progression via YAP1 activation [46]. Secondly, even though a wide range of cholesterol metabolism related genes have been studied in HCC, the role of FDPS in HCC remains largely uncharacterized and prior studies have lacked experimental investigation into its functional contribution and therapeutic relevance [47]. In this study, we conducted functional assays confirmed that FDPS knocking down disrupted cholesterol biosynthesis, suppressed tumor growth, and enhanced the efficacy of anti-PD-1 therapy. These new findings established FDPS as a key mediator of metabolic reprogramming and immune resistance in HCC, and highlighted it as a promising target for combinatorial strategies integrating metabolic inhibition with immunotherapy.

Additionally, from a methodological perspective, our study also partly addressed the limitations of conventional bioinformatic biomarker discovery approaches and proposes a more data-driven and disease-specific framework. Traditionally, pathway-based analyses rely on predefined gene sets derived from public databases such as GO, KEGG, and Reactome. While informative, these gene sets are typically curated based on general biochemical functions and not contextualized to specific diseases. As a result, such approaches present several drawbacks: (1) many included genes, except for well-characterized enzymes, may not be biologically relevant in a given disease, leading to potential false positives; (2) excessive reliance on existing gene sets limits the discovery of novel biomarkers that fall outside of canonical pathways; (3) these methods often lack a quantitative basis for assessing the relative contribution of individual genes to disease phenotypes, making it difficult to prioritize therapeutic targets [48]. However, in our study, the conventional cholesterol metabolism gene sets were used solely as a reference to stratify metabolic phenotypes at the single-cell level, resulting in the classification of HCholesterol, DTCholesterol, and LCholesterol malignant subgroups. Rather than relying on these predefined gene sets for downstream biomarker discovery, we subsequently applied disease- and cell-type-specific strategies, including hdWGCNA and single-cell machine learning, to refine and prioritize key drivers of cholesterol metabolic reprogramming. This approach effectively addresses the first two aforementioned limitations of traditional pathway-based analyses. Firstly, it circumvents the inclusion of biologically irrelevant genes that may appear in general databases but lack disease specificity, thereby reducing the risk of false positives. Secondly, it enables *de novo* identification of context-specific markers beyond canonical annotations. Moreover, the frequency with which a gene is selected across multiple machine learning models or its importance within model parameters offers a semi-quantitative estimation of its contribution to the metabolic phenotype, providing a more nuanced and data-driven basis for functional prioritization.

Despite the valuable insights, several limitations should be acknowledged. First, although scMetabolism and MetabolismExplorer provide robust tools for metabolic profiling, the influence of cell cycle dynamics and technical confounders may introduce biases in the metabolic signatures observed in this study.

In addition, our analyses were based on treatment-naïve ICB samples due to the unavailability of suitable HCC cohorts with matched pre- and post-ICB transcriptomic data. This limitation prevented a direct evaluation of therapy-induced metabolic reprogramming.

Apart from that, while FDPS inhibition is expected to impair protein prenylation of Ras and Rho family GTPases and thus attenuate downstream AKT/ERK signaling, we did not measure GTPase prenylation status or kinase phosphorylation in our experiments. Therefore, the proposed prenylation–AKT/ERK axis is inferred based on established mevalonate pathway biology and prior studies and requires further biochemical validation.

Moreover, FDPS functions at a critical metabolic branch point that controls both cholesterol biosynthesis and the production of isoprenoid intermediates essential for protein

prenylation. The observed antitumor and immunotherapy-sensitizing effects of FDPS inhibition may reflect a combined outcome of sterol depletion and impaired oncogenic signaling. However, we did not directly examine the contribution of these two branches, and future studies with metabolic rescue experiments (e.g., using FPP, GGPP, or cholesterol) will help delineate their relative roles.

Also, even though immunodeficient models or statin comparators could provide insights into the tumor cell-intrinsic effects of cholesterol biosynthesis inhibition, our study was designed to assess FDPS inhibition in immune-intact models to capture tumor-immune interactions. Whether FDPS targeting remains effective in immunodeficient settings or can be reproduced by upstream cholesterol blockade requires further investigation.

From a translational perspective, while alendronic acid is a clinically approved FDPS inhibitor with preferential accumulation in bone tissue, its pharmacodynamic effects in liver tumors are not fully characterized. Specifically, further metabolic and biochemical investigations are needed to determine whether FDPS inhibition alters isoprenoid intermediates or disrupts protein prenylation in hepatic tumors. Although no overt histopathological abnormalities or body weight loss were observed, a comprehensive evaluation of serum biochemical and hematological parameters was not conducted, limiting the safety assessment to an absence of overt toxicity under experimental conditions.

Finally, cholesterol metabolism is regulated at multiple levels, including epigenetic, post-transcriptional, and post-translational mechanisms. Incorporating additional omics modalities, such as proteomics, metabolomics, or spatial transcriptomics, would provide a more comprehensive and spatially resolved understanding of cholesterol metabolism within the tumor microenvironment.

5 Conclusion

In summary, our study provides a comprehensive single-cell resolution map of cholesterol metabolism in HCC and uncovers marked intratumoral heterogeneity linked to therapy resistance. Through integrative network analysis and machine learning, we identified FDPS as a central mediator of cholesterol metabolic reprogramming and a promising therapeutic target. Functional validation demonstrated that inhibiting FDPS not only impaired tumor growth but also sensitized tumors to anti-PD-1 immunotherapy. These findings highlight the potential of combining metabolic intervention with immune checkpoint blockade to improve outcomes in HCC, and offer a robust methodological framework for future biomarker discovery in oncology.

Supplementary Information The online version contains supplementary material available at https://doi.org/10.1007/s13402-026-01177-7.

Acknowledgements We acknowledge and thank the TCGA data portal, UCSC Xena data portal, and all researchers who generously shared their valuable sequencing data, which made this study possible.

Author contributions Conceptualization, Q.G. and M.Z.; methodology, X.Y., and J.L.; software, X.Y., and J.L; validation, X.Y., and J.L; investigation, X.Y., J.L. and Y.W.; formal analysis, X.Y., and J.L.; writing-original draft, X.Y., J.L., Y.W., Q.G. and M.Z.; writing-review & editing, X.Y., J.L. Q.G. and M.Z; visualization, X.Y. and J.L.; and supervision, Q.G. and M.Z.

Funding This work was not supported by any funding.

Data availability Data and code will be made available on request.

Declarations

Ethical approval All animal experiments were conducted in accordance with institutional guidelines and were approved by the Institutional Animal Care and Use Committee (IACUC) of the Shanghai Branch of Beijing Vital River Laboratory Animal Technologies Co., Ltd.

Competing interests The authors declare no competing interests.

References

1. M.R. Toh et al., Global epidemiology and genetics of hepatocellular carcinoma. Gastroenterology. **164**(5), 766–782 (2023)
2. X. Yang et al., Precision treatment in advanced hepatocellular carcinoma. Cancer Cell. **42**(2), 180–197 (2024)
3. C. Yang et al., Evolving therapeutic landscape of advanced hepatocellular carcinoma. Nat. Rev. Gastroenterol. Hepatol. **20**(4), 203–222 (2023)
4. C. Yang et al., Targeting the immune privilege of tumor-initiating cells to enhance cancer immunotherapy. Cancer Cell. **42**(12), 2064–2081 (2024). e19
5. N.N. Pavlova, J. Zhu, C.B. Thompson, The hallmarks of cancer metabolism: still emerging. Cell. Metab. **34**(3), 355–377 (2022)
6. D. Hanahan, Hallmarks of cancer: new dimensions. Cancer Discov. **12**(1), 31–46 (2022)

7. I. Elia, M.C. Haigis, Metabolites and the tumour microenvironment: from cellular mechanisms to systemic metabolism. Nat. Metab. **3**(1), 21–32 (2021)
8. X. Liu et al., Dysregulation of cholesterol metabolism in cancer progression. Oncogene. **42**(45), 3289–3302 (2023)
9. H. Xu et al., Cholesterol metabolism: new functions and therapeutic approaches in cancer. Biochim. Biophys. Acta Rev. Cancer. **1874**(1), 188394 (2020)
10. J. Luo, H. Yang, B.L. Song, Mechanisms and regulation of cholesterol homeostasis. Nat. Rev. Mol. Cell. Biol. **21**(4), 225–245 (2020)
11. L. Goicoechea et al., Mitochondrial cholesterol: metabolism and impact on redox biology and disease. Redox Biol. **61**, 102643 (2023)
12. B. Paul, M. Lewinska, J.B. Andersen, Lipid alterations in chronic liver disease and liver cancer. JHEP Rep. **4**(6), 100479 (2022)
13. X. Zhang et al., Dietary cholesterol drives fatty liver-associated liver cancer by modulating gut microbiota and metabolites. Gut. **70**(4), 761–774 (2021)
14. J. Huang et al., TMEM147 aggravates the progression of HCC by modulating cholesterol homeostasis, suppressing ferroptosis, and promoting the M2 polarization of tumor-associated macrophages. J. Exp. Clin. Cancer Res. **42**(1), 286 (2023)
15. J. Li et al., Chaperonin containing TCP1 subunit 5 as a novel pan-cancer prognostic biomarker for tumor stemness and immunotherapy response: insights from multi-omics data, integrated machine learning, and experimental validation. Cancer Immunol. Immunother. **74**(7), 224 (2025)
16. Y. Hong et al., Decoding per- and polyfluoroalkyl substances (PFAS) in hepatocellular carcinoma: a multi-omics and computational toxicology approach. J. Transl Med. **23**(1), 504 (2025)
17. Y. Xu et al., Integrating single-cell RNA sequencing and Spatial transcriptomics to reveal the Glycolysis-related gene GPRC5A as a potential biomarker for gastric cancer by machine learning. Int. J. Biol. Macromol. **323**(Pt 1), 147059 (2025)
18. S. Morabito et al., HdWGCNA identifies co-expression networks in high-dimensional transcriptomics data. Cell. Rep. Methods. **3**(6), 100498 (2023)
19. Z. Liu et al., Machine learning-based integration develops an immune-derived LncRNA signature for improving outcomes in colorectal cancer. Nat. Commun. **13**(1), 816 (2022)
20. R. Xue et al., Liver tumour immune microenvironment subtypes and neutrophil heterogeneity. Nature. **612**(7938), 141–147 (2022)
21. S.M. Kim et al., Sixty-five gene-based risk score classifier predicts overall survival in hepatocellular carcinoma. Hepatology. **55**(5), 1443–1452 (2012)
22. S. Boyault et al., Transcriptome classification of HCC is related to gene alterations and to new therapeutic targets. Hepatology. **45**(1), 42–52 (2007)
23. S. Roessler et al., A unique metastasis gene signature enables prediction of tumor relapse in early-stage hepatocellular carcinoma patients. Cancer Res. **70**(24), 10202–10212 (2010)
24. O.V. Grinchuk et al., Tumor-adjacent tissue co-expression profile analysis reveals pro-oncogenic ribosomal gene signature for prognosis of resectable hepatocellular carcinoma. Mol. Oncol. **12**(1), 89–113 (2018)
25. C. Yang et al., A survey of optimal strategy for signature-based drug repositioning and an application to liver cancer. Elife. **11**, (2022)
26. E. Villa et al., Neoangiogenesis-related genes are hallmarks of fast-growing hepatocellular carcinomas and worst survival. Results from a prospective study. Gut. **65**(5), 861–869 (2016)
27. Z. Zhou et al., Single cell atlas reveals multilayered metabolic heterogeneity across tumour types. EBioMedicine. **109**, 105389 (2024)
28. W. Wang et al., Integrating single-cell and bulk RNA sequencing data unveils antigen presentation and process-related CAFS and establishes a predictive signature in prostate cancer. J. Transl Med. **22**(1), 57 (2024)
29. Y. Sun et al., Single-cell HdWGCNA reveals metastatic protective macrophages and development of deep learning model in uveal melanoma. J. Transl Med. **22**(1), 695 (2024)
30. M. Elosua-Bayes et al., SPOTlight: seeded NMF regression to deconvolute Spatial transcriptomics spots with single-cell transcriptomes. Nucleic Acids Res. **49**(9), e50 (2021)
31. Y. Wu et al., Spatiotemporal immune landscape of colorectal cancer liver metastasis at Single-Cell level. Cancer Discov. **12**(1), 134–153 (2022)
32. S. Hanzelmann, R. Castelo, J. Guinney, GSVA: gene set variation analysis for microarray and RNA-seq data. BMC Bioinform. **14**, 7 (2013)
33. A. Butler et al., Integrating single-cell transcriptomic data across different conditions, technologies, and species. Nat. Biotechnol. **36**(5), 411–420 (2018)
34. P.S. Reel et al., Using machine learning approaches for multi-omics data analysis: A review. Biotechnol. Adv. **49**, 107739 (2021)
35. Y. Mao et al., Metabolic reprogramming, sensing, and cancer therapy. Cell. Rep. **43**(12), 115064 (2024)
36. J. Lin et al., Metabolic reprogramming in the tumor microenvironment of liver cancer. J. Hematol. Oncol. **17**(1), 6 (2024)
37. R.J. King, P.K. Singh, K. Mehla, The cholesterol pathway: impact on immunity and cancer. Trends Immunol. **43**(1), 78–92 (2022)
38. B. Huang, B.L. Song, C. Xu, Cholesterol metabolism in cancer: mechanisms and therapeutic opportunities. Nat. Metab. **2**(2), 132–141 (2020)
39. Y. Li et al., 7-Dehydrocholesterol dictates ferroptosis sensitivity. Nature. **626**(7998), 411–418 (2024)
40. J. Kopecka et al., Phospholipids and cholesterol: inducers of cancer multidrug resistance and therapeutic targets. Drug Resist. Updat. **49**, 100670 (2020)
41. H.M. Berman et al., The protein data bank. Nucleic Acids Res. **28**(1), 235–242 (2000)
42. J. Liu et al., Farnesyl diphosphate synthase exacerbates nonalcoholic steatohepatitis via the activation of AHR-CD36 axis. FASEB J. **37**(7), e23035 (2023)
43. S. Griffin, G. Preta, I.M. Sheldon, Inhibiting mevalonate pathway enzymes increases stromal cell resilience to a cholesterol-dependent Cytolysin. Sci. Rep. **7**(1), 17050 (2017)
44. W. Chen et al., The potential role and mechanism of circRNA/miRNA axis in cholesterol synthesis. Int. J. Biol. Sci. **19**(9), 2879–2896 (2023)
45. J. Wen et al., Targeting squalene epoxidase restores anti-PD-1 efficacy in metabolic dysfunction-associated steatohepatitis-induced hepatocellular carcinoma. Gut. **73**(12), 2023–2036 (2024)
46. K. Li et al., CSN6-SPOP-HMGCS1 axis promotes hepatocellular carcinoma progression via YAP1 activation. Adv. Sci. (Weinh). **11**(14), e2306827 (2024)
47. L. Tang et al., Establishment and validation of a cholesterol metabolism-related prognostic signature for hepatocellular carcinoma. Comput. Struct. Biotechnol. J. **20**, 4402–4414 (2022)
48. D. Mao et al., Integrated bioinformatics analysis identified cuproptosis-related hub gene Mpeg1 as potential biomarker in spinal cord injury. Sci. Rep. **15**(1), 1993 (2025)